https://doi.org/10.1038/s44384-026-00078-1

Single-particle limit of a topological edge state in a locally resonant band gap

Check for updates

Garigipati Sai Srikanth[1,6], Kai Qian[2,3,6], Ian Frankel[2,6], Georgios Theocharis[4], Nicholas Boechler[2,5] & Rajesh Chaunsali[1] ✉

Topological metamaterials promise unprecedented wave control. We theoretically and numerically investigate a one-dimensional Su–Schrieffer–Heeger (SSH)-inspired stiffness dimer modified with a local resonator, which imparts a frequency-dependent effective stiffness to the unit cell. The resonator introduces an attenuation singularity: at the frequency where the effective stiffness vanishes, the spatial attenuation of waves diverges. By tuning a dimerization parameter, we migrate this singularity from one band gap to the other via an intermediate flat-band state, transferring the dominant local-resonance character between the gaps without closing either gap while preserving the band topology. Crucially, when the resulting topological edge state intersects this singularity, it collapses onto a single boundary particle, forming a single-particle mode (SPM). This yields an inverse participation ratio of exactly unity, the theoretical limit for localization in a discrete system. Moreover, this extreme localization can be realized at low frequencies, below the first Bragg-type band gap. Further, we demonstrate that while random disorder detunes this mode, merely tuning the boundaries stabilizes the single-particle mode over a broad parameter range. Our findings provide a clear pathway to designing ultra-localized edge states in low-frequency regimes, where band topology guarantees the edge mode and local resonance drives its single-particle confinement.

Engineered materials, such as phononic crystals and acoustic metamaterials, provide powerful platforms for controlling wave propagation. One of their defining features is the ability to create frequency band gaps—spectral ranges where wave propagation is attenuated. These band gaps typically arise through two distinct physical mechanisms. The first is Bragg scattering, where coherent scattering from a periodic lattice opens so-called Bragg-type band gaps (BrGs)[1]. The second is local resonance, achieved by embedding resonant substructures into a host medium. These local resonators give rise to effective material properties (e.g., dynamic mass density or modulus) that can vanish or diverge at characteristic frequencies, creating locally resonant band gaps (LRGs)[2–7]. Beyond their differing physical origins, the two gap types differ in two key respects. Locally resonant band gaps can exhibit theoretically infinite attenuation (in contrast to the finite attenuation of BrGs for non-vanishing stiffnesses)[8–10]. Locally resonant gaps can also be positioned at lower frequencies than BrGs while maintaining other properties, such as a high long-wavelength sound speed (wherein the resonators can be deeply "sub-wavelength"[11 12] and the gap frequency "sub-Bragg"[13]).

Parallel to these developments, the introduction of topological band theory into mechanical systems has catalyzed the vibrant field of topological mechanics[14 15]. In these systems, robust boundary modes (or states) emerge at edges[16], interfaces[17], and corners[18]. Residing deep within band gaps, these states exhibit remarkable resilience to disorder and imperfections due to their underlying topological protection. This intrinsic robustness makes them prime candidates for next-generation applications in fault-tolerant, one-way passive waveguiding, logic, and signal processing. These topological boundary modes pair naturally with local resonance; the sharp attenuation of LRGs offers a route to edge localization complementary to Bragg-gap confinement. While BrG edge modes decay exponentially over broad parameter ranges, an LRG introduces an attenuation singularity that can drive extreme confinement at a specific frequency, motivating our study of resonance-assisted edge localization in topological metamaterials.

Localized boundary modes with topological origin have been previously reported in band gaps stemming from local resonance. For

[1]Department of Aerospace Engineering, Indian Institute of Science, Bengaluru, India. [2]Department of Mechanical and Aerospace Engineering, University of California, San Diego, CA, USA. [3]George W. Woodruff School of Mechanical Engineering, Georgia Institute of Technology, Atlanta, GA, USA. [4]Laboratoire d'Acoustique de l'Université du Mans (LAUM), UMR 6613, Institut d'Acoustique – Graduate School (IA-GS), CNRS, Le Mans, France. [5]Program in Materials Science and Engineering, University of California, San Diego, CA, USA. [6]These authors contributed equally: Garigipati Sai Srikanth, Kai Qian, Ian Frankel.
✉e-mail: rchaunsali@iisc.ac.in

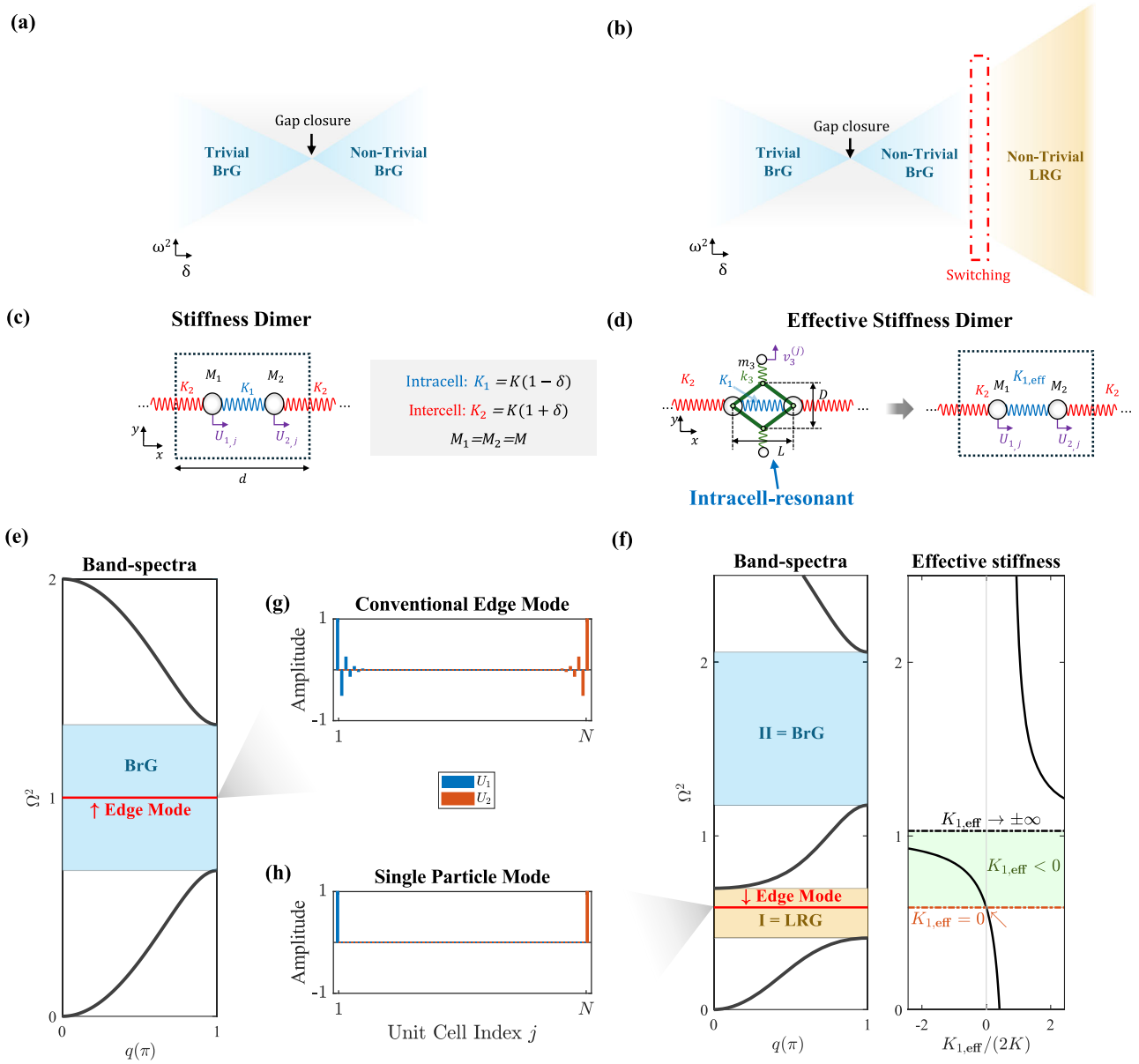


Fig. 1 | Comparison of topological edge modes in a Bragg-type band gap (BrG) and an effective stiffness, locally resonant band gap (LRG). a Band closure and reopening driving topological transition in a BrG. **b** Pathway to topologically non-trivial LRG via gap-type switching from a non-trivial BrG. **c** Unit cell of conventional stiffness dimer chain. **d** Unit cell of effective stiffness dimer chain with local resonators (m_3, k_3). **e** Band structure of conventional dimer; blue region denotes BrG, red line indicates edge mode. **f** Left: Band structure of effective stiffness dimer with BrG (blue, II) and LRG (yellow, I). Right: $K_{1,\text{eff}}$ versus a normalized $\Omega^2 = \omega^2 M/(K_1 + K_2)$; orange dashed line marks $K_{1,\text{eff}} = 0$. **g** Edge mode profile in conventional dimer showing exponential decay. **h** Single-particle mode (SPM), localized on the edge with IPR = 1, in the effective stiffness dimer. Parameters: $K_1 = 1$, $K_2 = 1.4286$, $M = 1$, $k_3 = 0.5$, $m_3 = 0.2$, $\lambda = 1$, $N = 60$ unit cells with fixed boundaries.

example, Zhang et al.[19] introduced resonator pairs into a classical valley-Hall lattice to obtain edge modes in resonant ranges, and Xia et al.[20] demonstrated edge modes in a beam with quasi-periodically attached resonators. However, until recently, the mechanism governing the topological transition from a trivial to a non-trivial LRG remained unclear. Conventional topological states at finite frequencies arise through band inversion at Dirac points, requiring gap closure and reopening [Fig. 1a]. In LRGs, by contrast, the attenuation singularity—associated with vanishing effective stiffness (equivalently, diverging effective mass)—enforces a non-vanishing minimum gap width[21], thereby preventing gap closure under continuous parameter tuning[22]. A recent study by Jang et al.[23] resolved this through a two-step process: first inducing a topological transition within a BrG, and subsequently switching its gap character to an LRG, thus bypassing the need for gap closure within the LRG itself [Fig. 1b]. Similarly, Zhang et al.[24] illustrated a BrG-to-LRG transition in a beam-resonator system. Notably, Jang et al.[23] also showed that the topological edge state formed at the local-resonance frequency, where the effective mass diverges, is confined to a single unit cell, forming a *singular edge mode*. This raises the questions that we address here: what is the theoretical limit of such localization—can a topological edge state be confined to a single *particle* (i.e., sub-unit-cell localization)? Further, can this be achieved in a low-frequency LRG, below the first BrG?

We answer these questions with a three-band effective stiffness model —namely, a modified version of the conventional SSH-inspired stiffness dimer chain [the main chain, composed of equal masses connected by alternating springs, as shown in Fig. 1c], where a truss-based local resonator is attached to the intracell spring [as shown in Fig. 1d, which we refer to as the *effective stiffness dimer chain*]. We show that, as a stiffness-dimerization

parameter is swept, the attenuation singularity (zero effective stiffness) introduced by the resonator crosses from one band gap to the other precisely when an intervening flat band forms, transferring the dominant local-resonance character between the gaps while preserving the band topology. The resulting topologically non-trivial gap, which we will herein refer to as an LRG (see the Results subsection 'Band gap characterization and switching' for the subtleties of this terminology), hosts topological edge modes. When such an edge state intersects the attenuation singularity, it becomes confined to a single particle at the boundary, forming what we term the *single-particle mode* (SPM)—the sub-unit-cell limiting case of the singular edge mode. This confinement represents the theoretical maximum of localization in a discrete system and, to the best of our knowledge, has not been demonstrated previously. Further, we are able to achieve this SPM at low frequencies, below the first BrG, by leveraging the aforementioned advantages conferred by local resonance. Finally, we demonstrate that, by simple tuning of the boundary stiffness, the SPM can be maintained over a finite range of unit-cell parameters, rather than only at a fine-tuned resonance condition, even with random disorder in the chain.

The remainder of this paper is organized as follows. The Results section details the band gap characterization and switching mechanism, analyzes the topological transition via band inversion, examines the finite chain spectrum and edge state localization, and discusses disorder analysis and tuned boundaries. The Discussion section provides a summary and outlook. The Methods section presents the unit-cell dynamics and the effective model, the finite-chain eigenvalue problem, and the disorder scheme.

Results

Our system is a quasi-one-dimensional diatomic lattice, as illustrated in Fig. 1d. The jth unit cell consists of two identical primary masses M, constrained to horizontal motion, with displacements denoted by $U_{1,j}$ and $U_{2,j}$. The primary masses are coupled by alternating linear springs of stiffness K_1 (intracell) and K_2 (intercell). The intracell spring is modified by a symmetric truss-type local-resonator structure proposed in ref. 25. This structure comprises a pair of identical local resonators, each consisting of a mass m_3 and a spring k_3, coupled to the main chain through a hinged, massless truss mechanism characterized by the geometric parameter $\lambda = L/D$. The resonator masses are constrained to vertical motion with displacement denoted by $v_{3,j}$. As a result, the intracell coupling becomes frequency dependent and is described by an effective stiffness $K_{1,\mathrm{eff}}(\omega)$ [Eq. (18), Methods], which diverges at the resonator natural frequency $\omega_r = \sqrt{k_3/m_3}$ and vanishes at a distinct frequency $\omega_s < \omega_r$.

Band gap characterization and switching

We analyze the band structure of the effective stiffness dimer chain (see Methods for the equations of motion and the effective-medium description) to understand wave propagation in our system and detail the mechanism for switching the band gap type [Fig. 1b]. To facilitate a systematic parameter study, we introduce a dimerization parameter δ, treated as a static structural parameter, and a constant stiffness scale K to define the physical alternating stiffnesses as

$$K_1 = K(1-\delta), \quad K_2 = K(1+\delta), \tag{1}$$

with $K > 0$ and $\delta \in (-1, 1)$. This isolates δ as the primary control parameter: positive δ corresponds to weaker intracell coupling relative to intercell coupling, and vice versa. We further introduce non-dimensional quantities to express our results in universal form: stiffness ratio $\kappa_3 = k_3/(2K)$; characteristic frequency $\omega_{\mathrm{mid}} = \sqrt{2K/M}$ (the mid-gap frequency of the unit cell without local resonators at $\delta = 0$); normalized resonator frequency $\Omega_r = \omega_r/\omega_{\mathrm{mid}}$; and normalized frequency $\Omega = \omega/\omega_{\mathrm{mid}}$, such that $\Omega^2 = \omega^2 M/(2K)$.

Before analyzing the switching mechanism, we clarify how we classify the band gaps. In their pure limits, the two gap types are cleanly separable: a pure BrG is set by the periodicity of the main chain and survives removal of the resonators, whereas a pure LRG is pinned to the resonator frequency and is insensitive to changes in the lattice constant[8,26]. At finite coupling between the resonators and the main chain, however, both mechanisms contribute to every gap, and each gap generically acquires a hybrid character; prior works, such as ref. 8, describe criteria for classifying such gaps. Here, we classify each gap by its dominant mechanism, using the attenuation singularity—a frequency at which the spatial decay rate of evanescent waves diverges [$\mathrm{Im}(q) \to \infty$, where q is the dimensionless Bloch wavenumber (see Methods)]—as the discriminant: a gap containing the singularity is local-resonance dominant, and we call it an LRG; a gap lacking it is Bragg dominant, and we call it a BrG. We adopt these operational definitions throughout this study. In our system, the attenuation singularity corresponds precisely to the vanishing of the effective stiffness, $K_{1,\mathrm{eff}} = 0$. To find this singular frequency, we set Eq. (18) to zero and solve for ω_s^2:

$$\omega_s^2 = \omega_r^2 \frac{K_1}{K_1 + \lambda^2 k_3/2} = \omega_r^2 \left(1 + \frac{\lambda^2 k_3}{2K_1}\right)^{-1}. \tag{2}$$

Substituting $K_1 = K(1-\delta)$ and $k_3 = 2K\kappa_3$, and normalizing by $\omega_{\mathrm{mid}}^2 = 2K/M$, we obtain:

$$\Omega_s = \Omega_r \left(1 + \frac{\lambda^2 \kappa_3}{1-\delta}\right)^{-1/2}. \tag{3}$$

Here, Ω_s denotes the normalized zero-effective-stiffness frequency associated with $K_{1,\mathrm{eff}} = 0$. Physically, when $K_{1,\mathrm{eff}} = 0$, the intracell coupling vanishes, effectively decoupling adjacent unit cells and preventing wave propagation entirely. Consistent with this classification, the gap containing Ω_s is thus the LRG. A conventional alternative for locating the BrG is the Bragg periodicity frequency Ω_p: the frequency at which a wave traveling at the long-wavelength sound speed of the chain has a wavelength equal to twice the lattice constant, so that Bragg scattering first becomes possible. We do not adopt this criterion because, once the two mechanisms overlap, Ω_p need not lie within the BrG (see the Supplementary Information section 'Bragg and local-resonance diagnostics for band gap classification', where Ω_p is derived and tested against Ω_s).

Figure 2 tracks the complex band structure evolution as δ is varied. We first define a particular dimerization parameter, δ_f, where the middle branch forms a flat band[27] with zero group velocity across the entire Brillouin zone. In Fig. 2a, where $\delta < \delta_f$, the upper gap (II) contains the singularity (orange dashed line where $\mathrm{Im}(q) \to \infty$), identifying it as an LRG. The lower gap (I) has a bounded, arch-shaped attenuation profile characteristic of Bragg scattering, identifying it as a BrG. As δ increases, the singularity migrates from gap II to gap I, so the gap character switches in the sense that the local-resonance attenuation singularity is transferred between the two gaps. This interchange occurs at $\delta = \delta_f$, derived by finding when the middle band becomes dispersionless (see Fig. 2b and the Supplementary Information section 'Analytical criteria for band-touching and flat band phenomena'):

$$\delta_f = \left(\frac{\kappa_3\lambda^2 + \Omega_r^2}{2}\right) - \sqrt{\left(\frac{\kappa_3\lambda^2 + \Omega_r^2}{2} - 1\right)^2 + 2\lambda^2\kappa_3}. \tag{4}$$

This flat band is a necessary intermediate state for singularity migration as the stiffness parameter δ is swept. Within a propagating band, the wavenumber q is strictly real, whereas the attenuation singularity belongs to the evanescent spectrum ($\mathrm{Im}(q) \to \infty$); a band of finite bandwidth therefore acts as a spectral barrier that the singularity cannot traverse. Only when the intervening band collapses to zero bandwidth—forming the flat band at $\delta = \delta_f$—does this barrier vanish, allowing the singularity to cross from one gap to the other[28,29]. At this switching point [Fig. 2b], gaps I and II are bridged only by the flat band and effectively merge into a single, larger gap, which we denote as a 'mixed' BrG–LRG following the convention of ref. 26 (as noted

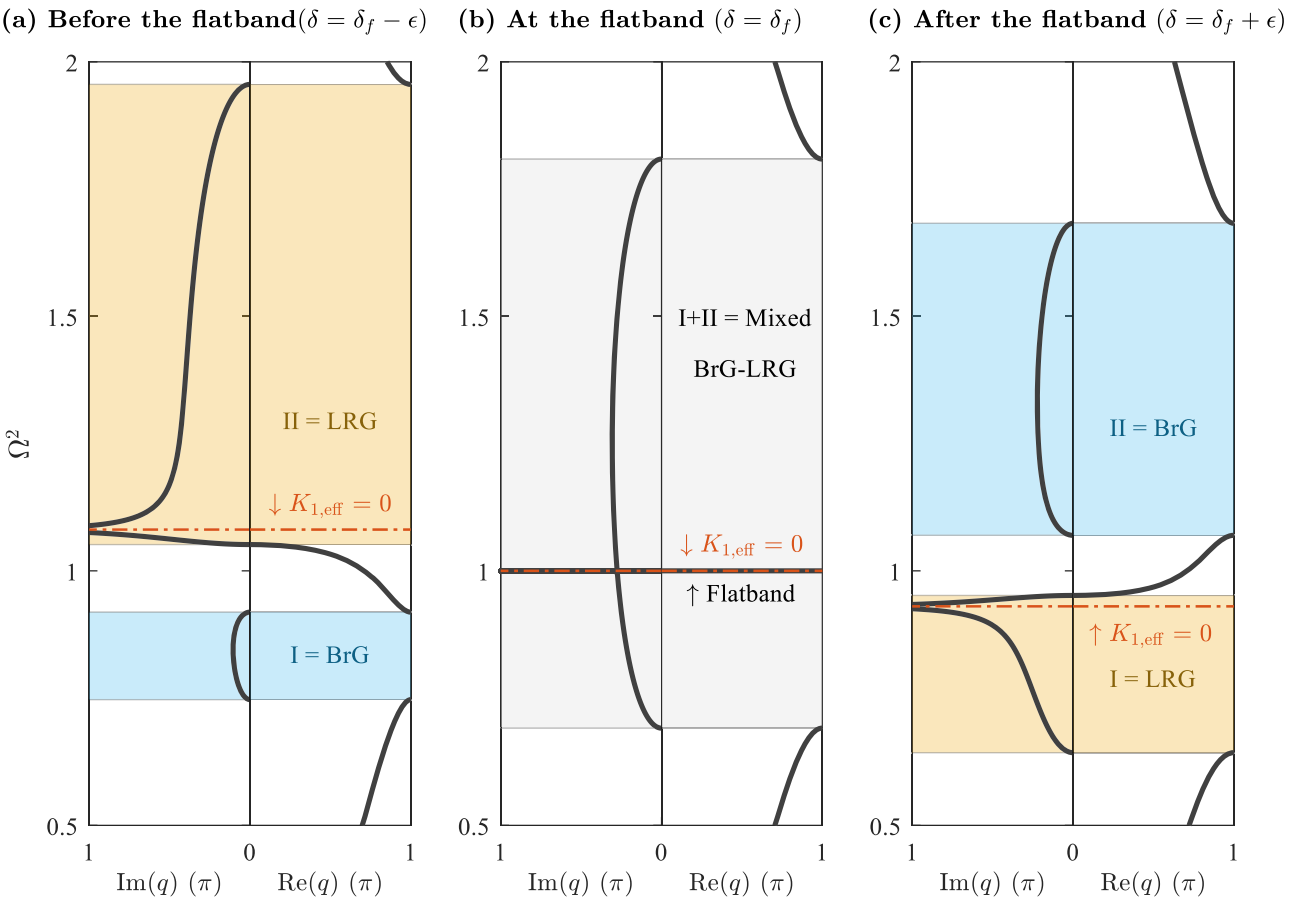


Fig. 2 | Band gap type switching via a flat band. Orange dashed line marks $K_{1,\mathrm{eff}} = 0$; its location defines LRG (yellow) versus BrG (blue). **a** $\delta < \delta_f$: singularity in upper gap (II = LRG). **b** $\delta = \delta_f$: singularity traversal through the flat band (the transitional `mixed' BrG--LRG state). **c** $\delta > \delta_f$: singularity in lower gap (I = LRG). Offset $\epsilon = 0.15\delta_f$ used in (**a**) and (**c**). Parameters: $K = 1$, $M = 1$, $k_3 = 0.5$, $m_3 = 0.2$, $\lambda = 1$.

previously, the other gaps could also be considered 'mixed' depending on the criteria used). For $\delta > \delta_f$ [Fig. 2c], the singularity then resides in gap I, making it the LRG, while gap II becomes a BrG—the reverse of the assignment for $\delta < \delta_f$. We emphasize that this flat-band–mediated migration is specific to the discrete model studied here; in continuum and flexural-beam systems, BrG–LRG switching has been reported without invoking flat-band formation[8].

Finally, we note where these gaps lie relative to the Bragg scale. For $\delta > \delta_f$, the singularity-hosting gap I sits below the BrG (gap II) and, depending on the resonator parameters, can even lie entirely below Ω_p, i.e., below the frequency at which Bragg interference first becomes possible; gaps in this regime are termed "sub-Bragg"[13]. Since the long-wavelength sound speed is set by the main chain alone (see the Supplementary Information section 'Bragg and local-resonance diagnostics for band gap classification'), the topological edge state analyzed below can reside in a low-frequency gap obtained without sacrificing the quasi-static stiffness of the chain.

Topological transition via band inversion

This subsection investigates the topological transitions arising from band gap closures—specifically, the formation of Dirac points—and the topological consequences of the gap-type switching discussed in the previous subsection. Our primary objective is to establish the conditions under which the LRG can host a topological phase.

To formally characterize the topology, we must first establish the relevant symmetries. The full 3×3 dynamical matrix $\mathbf{D}(q)$ [Eq. (16), Methods] is inversion symmetric [satisfying $\mathbf{PD}(q)\mathbf{P}^{-1} = \mathbf{D}(-q)$], with the parity operator given as (see the Supplementary Information section 'Inversion symmetry analysis'):

$$\mathbf{P} = \begin{pmatrix} 0 & -1 & 0 \\ -1 & 0 & 0 \\ 0 & 0 & 1 \end{pmatrix}. \tag{5}$$

This 3×3 structure complicates a direct mapping to the canonical Su–Schrieffer–Heeger (SSH) model. Here, the power of the effective medium framework becomes evident: the 2×2 effective dynamical matrix $\mathbf{D}_{\mathrm{eff}}(q)$ [Eq. (21), Methods] also preserves inversion symmetry, but in a form that allows us to utilize standard 1D topological invariants.

The inversion symmetry of the effective model is expressed as:

$$\boldsymbol{\sigma}_x \mathbf{D}_{\mathrm{eff}}(-q)\boldsymbol{\sigma}_x^{-1} = \mathbf{D}_{\mathrm{eff}}(q), \tag{6}$$

where the Pauli matrix $\boldsymbol{\sigma}_x$ acts as the inversion operator, swapping the two primary masses. At the high-symmetry points of the Brillouin zone ($q = 0$ and $q = \pi$), time-reversal symmetry imposes $\mathbf{D}_{\mathrm{eff}}(-q) = \mathbf{D}^*_{\mathrm{eff}}(q) = \mathbf{D}_{\mathrm{eff}}(q)$ since the matrix is real. Consequently, at these points, $\mathbf{D}_{\mathrm{eff}}$ commutes with the inversion operator $\boldsymbol{\sigma}_x$. This commutation dictates that the eigenvectors of the dynamical matrix can be chosen as simultaneous eigenvectors of $\boldsymbol{\sigma}_x$. Since the eigenvalues of $\boldsymbol{\sigma}_x$ are $+1$ and -1, the eigenvectors at these high-symmetry points are constrained to be either symmetric (parity $+1$) or antisymmetric (parity -1):

$$\mathbf{U}_{\mathrm{eff}}^{\mathrm{even}} \propto \begin{pmatrix} 1 \\ 1 \end{pmatrix} \quad \text{or} \quad \mathbf{U}_{\mathrm{eff}}^{\mathrm{odd}} \propto \begin{pmatrix} 1 \\ -1 \end{pmatrix}. \tag{7}$$

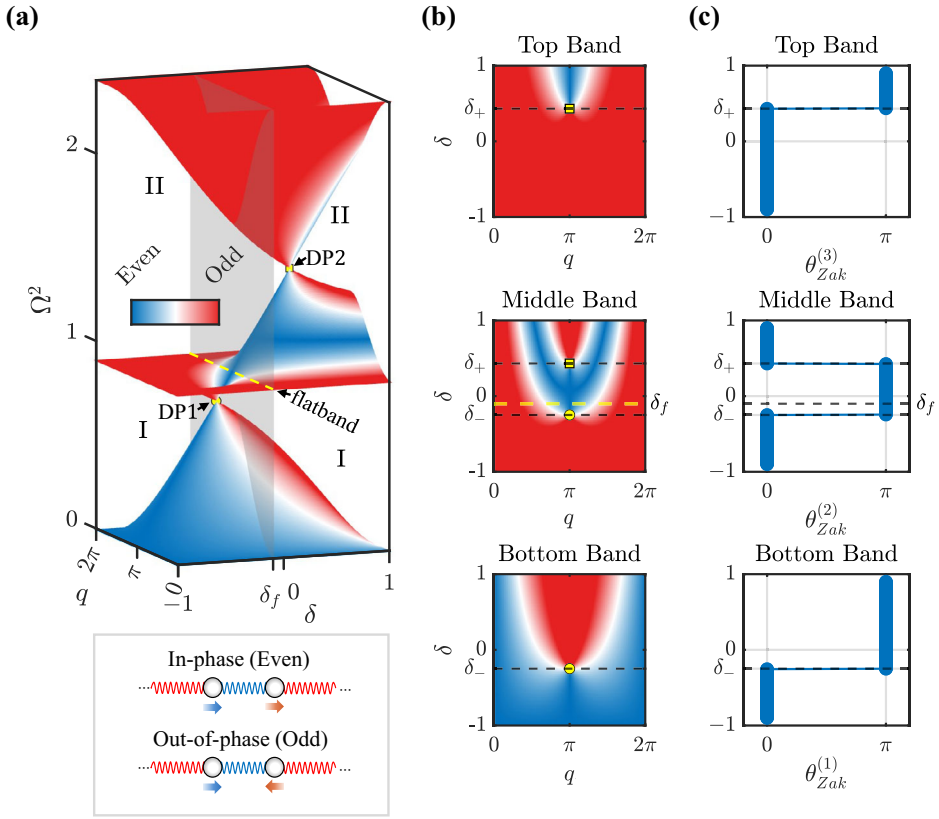


Fig. 3 | Topological phase transitions and band inversion. a Band structure evolution with δ. Color map: phase difference $|\arg(U_2) - \arg(U_1)|$ (in-phase = even = blue = 0, out-of-phase = odd = red = π). DP1/DP2 mark Dirac points; dashed yellow line and the vertical gray plane indicate the flatband and δ_f, respectively. **b** Phase along the Brillouin zone versus δ for each band; phase change along $q = \pi$ shows inversion at $\delta_\pm$. **c** Zak phase versus δ, confirming transitions only at $\delta_\pm$. Parameters: $K = 1$, $M = 1$, $k_3 = 0.43$, $m_3 = 0.2$, $\lambda = 1$.

This symmetry constraint provides a direct physical observable to probe the topology. Here, U_1 and U_2 denote the Bloch amplitudes of the two primary masses (see Methods). For a symmetric eigenvector, the two masses move in phase, and the phase difference is $|\arg(U_2) - \arg(U_1)| = 0$. For an antisymmetric eigenvector, they move in anti-phase, and the phase difference is $|\arg(U_2) - \arg(U_1)| = \pi$. Therefore, monitoring this phase difference across the Brillouin zone offers a direct map of the band's parity eigenvalues. A change in this quantized phase from 0 to π (or vice versa) between $q = 0$ and $q = \pi$ signals a band inversion and a non-trivial Zak phase.

Figure 3a visualizes this topology by plotting the phase difference $|\arg(U_2) - \arg(U_1)|$ for all bands. We observe band gap closures at two distinct Dirac points located at $q = \pi$: The first Dirac point (DP1) occurs at $\delta = \delta_-$ (inverting the bottom and middle bands), and the second Dirac point (DP2) occurs at $\delta = \delta_+$ (inverting the middle and top bands). These critical values correspond to the condition where two bands touch each other at the Brillouin zone boundary (see the Supplementary Information section 'Analytical criteria for band-touching and flat band phenomena' for the derivation):

$$\delta_\pm = \left(\frac{\kappa_3\lambda^2}{4} + \frac{\Omega_r^2 - 1}{2}\right) \pm \sqrt{\left(\frac{\kappa_3\lambda^2}{4} + \frac{\Omega_r^2 - 1}{2}\right)^2 + \frac{\lambda^2\kappa_3}{2}}. \quad (8)$$

The hierarchy of critical points is $\delta_- < \delta_f < \delta_+$. This establishes a clear sequence of transitions as δ increases: (i) a topological transition in the lower gap (I) via DP1 at δ_-; (ii) the BrG-to-LRG character switch at δ_f; and (iii) a topological transition in the upper gap (II) via DP2 at δ_+. In Fig. 3b, phase change is seen, via a change in the color plotted, along $q = \pi$ at $\delta = \delta_-$ and $\delta = \delta_+$.

To formally confirm these observations, we calculate the Zak phase for each band using the discrete formulation[30]:

$$\theta^{(b)}_{\text{Zak}} = -\text{Im}\ln\left[\prod_{r=0}^{R-1}\langle\psi_b(q_r)|\psi_b(q_{r+1})\rangle\right], \quad (|\psi_b(q_R)\rangle \equiv |\psi_b(q_0)\rangle), \quad (9)$$

Table 1 | Sign of topological gap invariant $\varsigma^{(b)}$ for intracell-resonant stiffness dimer chains.

	$\delta < \delta_-$	$\delta_- < \delta < \delta_+$	$\delta > \delta_+$
sgn[$\varsigma^{(I)}$]	−	+	+
sgn[$\varsigma^{(II)}$]	+	+	−

where $|\psi_b\rangle$ is the normalized eigenvector. As shown in Fig. 3c, the Zak phase jumps between 0 and π exactly at $\delta_\pm$, matching the phase difference analysis. Finally, we define the gap topological invariant $\varsigma^{(b)}$ as the sum of Zak phases for all bands below the gap[22,31]:

$$\text{sgn}[\varsigma^{(b)}] = (-1)^b \exp\left(i\sum_{m=1}^{b}\theta^{(m)}_{\text{Zak}}\right). \quad (10)$$

Table 1 summarizes these invariants. The most crucial finding here is the topological inheritance: the gap-type switching at δ_f does *not* alter the topological invariant. A gap that is topologically non-trivial as a BrG retains its non-trivial character even after it switches to become an LRG.

Finite chain spectrum and edge state localization, including the single-particle mode

We now analyze the eigenfrequency spectrum of a finite chain composed of $N = 60$ unit cells with fixed boundary conditions [Fig. 4a]. This analysis allows for the direct observation of topological edge states that emerge within the bulk band gaps and provides a platform to verify the bulk-boundary correspondence.

As a baseline, Fig. 4b shows the spectrum for a standard stiffness dimer (without local resonators, i.e., $K_{1,\text{eff}} = K_1$) as a function of δ. The bulk modes (black markers) form continuous bands separated by a single BrG (blue shaded region). This gap closes at $\delta = 0$ (the Dirac point) and reopens into a topologically distinct phase, giving rise to a mid-gap edge state (red

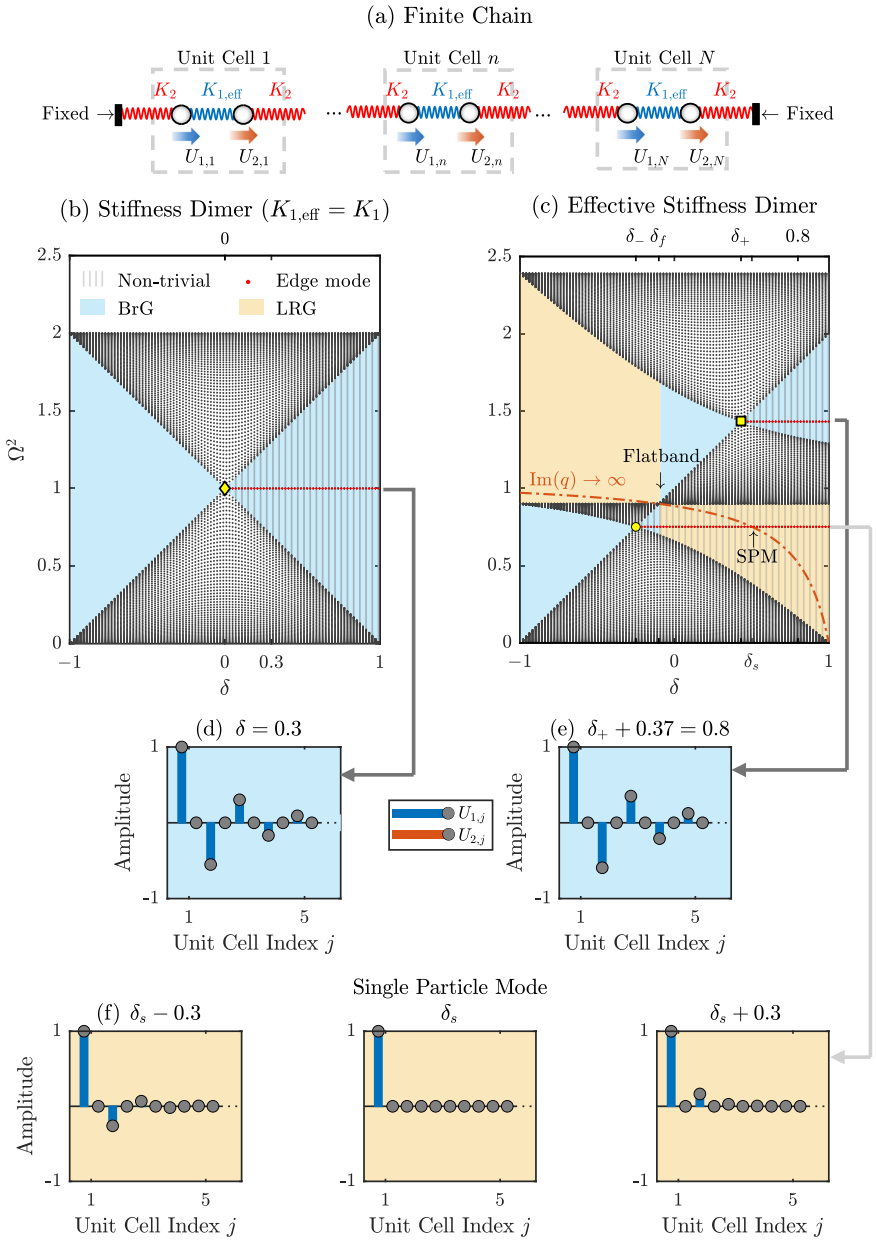


Fig. 4 | Finite-chain eigenspectra and edge states, including the single-particle mode. a Schematic of finite chain with fixed boundaries. **b** Standard dimer spectrum; edge modes (red markers) emerge for $\delta > 0$. **c** Effective stiffness dimer spectrum; orange curve marks $K_{1,\text{eff}} = 0$. Vertical lines: δ_-, δ_f, δ_+, and δ_s (in ascending order for these parameters). **d** Edge mode shape in standard dimer at $\delta = 0.3$. **e** Edge mode in upper BrG at $\delta = 0.37$. **f** Edge modes in lower LRG at $\delta_s - 0.3$, δ_s, and $\delta_s + 0.3$; center shows SPM (IPR = 1). Parameters: $K = 1, M = 1, k_3 = 0.43, m_3 = 0.2, \lambda = 1$, $N = 60$.

markers) for $\delta > 0$. The mode shape of this edge state, shown in Fig. 4d, exhibits the characteristic exponentially decaying profile with alternating signs between adjacent unit-cells, a hallmark of SSH-type topological modes.

For the intracell-resonant effective stiffness dimer chain, we solve the full finite eigenvalue problem [Eq. (22); see Methods for the construction of the finite-chain matrices]. The resulting spectrum is richer, as shown in Fig. 4c. We distinguish the band gap character by overlaying the frequency of the attenuation singularity (orange dashed curve), which marks the condition $K_{1,\text{eff}} = 0$. The band gap containing this singularity is the LRG (yellow region), while the gap without it is the BrG (blue region). The BrG-to-LRG switching event is clearly visible at $\delta = \delta_f$.

Consistent with the bulk topological analysis, topological edge states (red markers) emerge in each band gap once δ crosses the corresponding Dirac point. The lower gap (I) hosts an edge state for $\delta > \delta_-$, and the upper gap (II) hosts one for $\delta > \delta_+$. Figure 4e displays the mode shape for an edge state in the upper BrG (gap II). It shows localization similar to the standard stiffness dimer [Fig. 4d], with exponential decay and multi-site participation, specifically characterized by out-of-phase motion between alternating sites.

The lower LRG enables a novel localization phenomenon. When the frequency of the attenuation singularity, Ω_s, coincides with the frequency of the lower topological edge state, $\Omega_{\text{edge,I}}$ (derived in the Supplementary Information section 'Frequency of Edge States'), the SPM condition is met. This occurs at the specific value $\delta = \delta_s$ (see the Supplementary Information section 'Single-Particle Edge State Condition'):

$$\delta_s = \left(\frac{\kappa_3\lambda^2}{2} + \Omega_r^2\right) - \sqrt{\left(\frac{\kappa_3\lambda^2}{2} + \Omega_r^2 - 1\right)^2 + 2\kappa_3\lambda^2}. \qquad (11)$$

At this precise point, the topological state achieves extreme localization, as illustrated in Fig. 4f. The central panel of Fig. 4f ($\delta = \delta_s$) shows the mode shape confined entirely to a single primary mass at the chain's boundary, i.e., an SPM. This contrasts with the singular edge mode of ref. 23, which is confined to a single unit cell: here, the confinement is sub-unit-cell, collapsing onto one particle.

Across this point, a transition in the edge mode profile is observed: for $\delta < \delta_s$, the alternating sites oscillate out of phase as seen in the left panel of Fig. 4f, whereas for $\delta > \delta_s$, they oscillate in phase as seen in the right panel of Fig. 4f. Consequently, the SPM condition at $\delta = \delta_s$ serves as a singular crossover point between these distinct localization regimes. We quantify this localization using the inverse participation ratio (IPR), computed over the primary masses [Eq. (25), Methods]. For the SPM at $\delta = \delta_s$, the IPR is exactly unity—the theoretical maximum for localization in a discrete lattice—for a single boundary mode localized at either edge. This is reminiscent of the full dimerized limit of an SSH dimer[32], but here it occurs at a finite frequency within an LRG. This extreme confinement arises from three cooperating ingredients. The bulk topology (Zak phase) guarantees the edge mode and fixes its SSH-like nodal structure, placing zero amplitude on alternating particles; spectral isolation from the bulk bands sets its decay length; and the vanishing effective stiffness ($K_{1,\text{eff}} \to 0$) decouples the boundary unit cell from the rest of the chain—the local resonators precisely counterbalancing the inertial force of the boundary mass—collapsing the mode onto a single particle. Of these, only the existence of the edge mode is topologically guaranteed; the single-particle confinement follows from matching the edge-state frequency to $K_{1,\text{eff}} = 0$ and is therefore driven by local resonance rather than protected by topology. It is important to emphasize here the necessity of the locally resonant mechanism for such extreme mode localization. In a Bragg gap, unless one of the springs is driven to zero stiffness, the imaginary wave number remains finite. In locally resonant systems (whether mass or stiffness dimers), as mentioned, the attenuation can become infinite in an idealized, non-dissipative system.

This exact IPR = 1 value is a property of a small-amplitude linear eigenstate. Because the IPR characterizes the normalized modal profile rather than the absolute vibration amplitude, the state implies no large displacement, strain, or internal force, and the effective-stiffness description remains self-consistent in the infinitesimal-amplitude limit. It is therefore an idealized linear limit: in practice, geometric, material, or inertial nonlinearities and fabrication imperfections may shift the exact $K_{1,\text{eff}} = 0$ condition, but it nonetheless provides a clear design target for approaching extremely localized edge states.

We also emphasize the value of locating the edge state in the LRG from a design perspective: it frees the prescription of edge-mode frequencies from other structural constraints. Locally resonant band gaps have been suggested to have particular value in creating forbidden regions at extremely low frequencies, below the first Bragg gap of the main chain. Contrasting against systems that exhibit pure Bragg gaps, we highlight two scenarios. First, consider a scenario where a specific mass budget is available for a system and a minimum quasi-static stiffness of the system is required. In a monoatomic or diatomic spring-mass chain, these parameters dictate the frequency of the Bragg gap. If one then adds local resonators, such as in a negative effective mass model[33], then by allocating mass to the local resonator an extremely low-frequency band gap can be enabled via a small stiffness of the local resonator. Second, imagine a scenario where a high long-wavelength sound speed is required. As highlighted in the Supplementary Information, in our locally resonant stiffness dimer system, the long-wavelength sound speed is dictated by the main chain mass, stiffness, and unit cell length. These same parameters pin the Bragg gap at high frequencies, whereas the parameters of the local resonator can be tuned to enable an arbitrarily low-frequency band gap.

Disorder analysis and tuned boundaries

Having established the SPM at $\delta = \delta_s$, we now address two practical questions: (i) how robust is this extreme localization to structural disorder, and (ii) can the single-particle confinement be extended from an isolated fine-tuned point to a continuous parameter range? These questions are central to any experimental realization: although the bulk topology guarantees the edge mode, the IPR = 1 confinement requires matching its frequency to $K_{1,\text{eff}} = 0$, so it is sensitive to detuning by the imperfections present in any real structure. We address both through a disorder analysis and a boundary-tuning strategy, showing that boundary tuning not only broadens the SPM into a finite parameter window but also improves its resilience to random perturbations by spectrally isolating the mode from the bulk bands.

We first assess the effect of random disorder on the SPM, assigning independent random variations to every stiffness element in the finite chain (K_1, K_2, and k_3; see Methods for the disorder scheme). Figure 5 presents a comparative study of localization, quantified by the IPR, across different configurations. Figure 5a serves as the reference case (no disorder), showing the sharp peak in IPR reaching exactly unity at $\delta = \delta_s$ for mode numbers 60 and 61 (where the modes are arranged in an ascending order of eigenfrequencies). When 10% disorder is introduced [Fig. 5b], the translational symmetry is broken, and the eigenfrequencies of the edge modes scatter around the theoretical prediction. While the perfect IPR = 1 condition is perturbed, the edge mode shows a degree of intrinsic robustness as it retains high localization values near δ_s.

To overcome the limitation of the SPM being created at a single design point δ_s, and to realize it across a broader range of system configurations, we propose a "tuned boundary" strategy. The physical intuition is to enforce the SPM condition locally at the boundaries, regardless of the bulk parameters. We achieve this by modifying the stiffness of the boundary springs ($K_{2,1}$ at the left edge and $K_{2,N+1}$ at the right edge) such that the natural frequency of the isolated boundary mass matches the frequency where the bulk effective stiffness vanishes (*i.e.*, ω_s). This requires satisfying the condition $K_{2,\text{boundary}}/M = \omega_s^2$, where $K_{2,\text{boundary}}$ denotes the stiffness of either boundary spring. This condition yields the closed-form tuning expressions:

$$K_{2,1} = \frac{Mk_{3,1}}{m_3\left(1 + \frac{\lambda^2 k_{3,1}}{2K_{1,1}}\right)}, \quad K_{2,N+1} = \frac{Mk_{3,N}}{m_3\left(1 + \frac{\lambda^2 k_{3,N}}{2K_{1,N}}\right)}. \tag{12}$$

Here, $K_{1,1}$, $k_{3,1}$ and $K_{1,N}$, $k_{3,N}$ denote the intracell and resonator stiffnesses of the first and Nth unit cells, respectively (site-indexed stiffnesses are defined in Methods). This tuning effectively "pins" the edge mode to the attenuation singularity curve ($K_{1,\text{eff}} = 0$) across the parameter space. We note that this creates a "defective" boundary which does not support a topological edge mode in a strict sense; however, we suggest this is of interest regarding preservation of the single-particle localized edge mode. Previously, Yousef et al.[34] have tuned eigenfrequencies of edge modes in a BrG by tuning the edges. To the best of our knowledge, such a study in LRGs or its impact on localization remains unexplored. The efficacy of this strategy is demonstrated in Fig. 5c. With tuned boundaries (and no disorder), the edge mode frequency perfectly tracks the orange dashed line corresponding to the attenuation singularity. Consequently, the edge mode maintains an IPR of exactly 1 over a broad range of δ, extending the SPM from a point-like phenomenon to a stable phase across a parameter space. Note that this tuning modifies the boundary conditions sufficiently to close the gap for BrG-based edge modes, which disappear, while new edge modes appear in gap I for $\delta < \delta_-$.

This boundary pinning also protects the SPM against disorder, provided the mode stays spectrally isolated from the bulk. Figure 5d shows the tuned system subject to 10% disorder, revealing two distinct regimes. In the "Mixing" region, where the edge-mode frequency (tracking $K_{1,\text{eff}} = 0$) approaches the bulk bands, disorder drives hybridization between the edge state and bulk modes, leading to delocalization. In the "No mixing" region, by contrast, where the attenuation singularity is well separated from the bulk spectrum, the tuned SPM is markedly resilient: the IPR stays close to unity and the mode remains spectrally distinct despite significant structural randomness. This resilience is a direct consequence of spectral isolation—keeping the edge mode far from the bulk bands suppresses disorder-induced hybridization. The combination of spectral separation and boundary tuning thus provides a practical route to ultra-localized states in imperfect metamaterials whose edge modes originate from band topology.

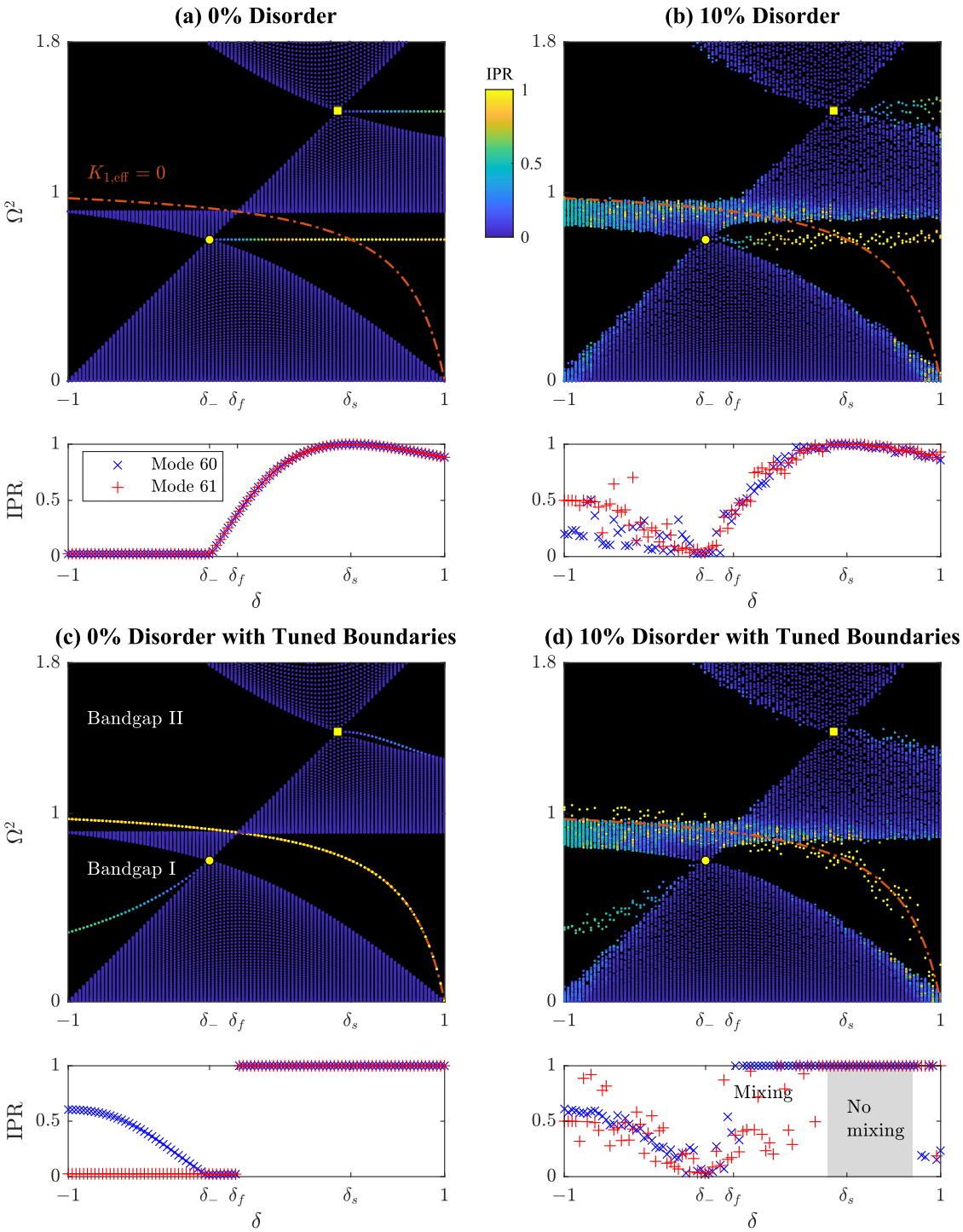


Fig. 5 | Localization and disorder with tuned boundaries. IPR shown by color (yellow = 1, blue = minimum). Lower panels: IPR for modes 60 and 61 (LRG edge modes). **a** No disorder: IPR → 1 at δ_s. **b** 10% disorder: frequencies scatter but high IPR maintained near δ_s. **c** Tuned boundaries, no disorder: edge modes track $K_{1,\text{eff}} = 0$, achieving IPR = 1 broadly. **d** Tuned boundaries, 10% disorder: SPM in "No mixing" region; hybridization in "Mixing" region.

Discussion

In this work, we introduced a locally resonant stiffness dimer as a framework for generating topological edge states within LRGs. By mapping the lattice to an effective medium, we identified the attenuation singularity—where the effective stiffness vanishes—as the operational signature of the LRG. We then showed that this singularity can be controllably migrated between adjacent band gaps by tuning a dimerization parameter, transferring the dominant local-resonance character—and hence the LRG designation—to the host gap. Crucially, flat-band formation mediates this migration, with a 'mixed' BrG–LRG gap appearing at the transition point. Overall, this process preserves the topological invariant (the Zak phase): the system inherits non-trivial topology from a BrG without the gap closure usually required for topological transitions in LRGs.

A central finding herein is the single-particle mode (SPM). When a topological edge state spectrally intersects the local-resonance-induced attenuation singularity, the vibrational energy collapses onto a single boundary particle, reaching an IPR = 1—the theoretical limit for localization in a discrete lattice. This sharpens the single-unit-cell ('singular') edge mode

of ref. 23 to its ultimate sub-unit-cell limit. We posit that the band topology guarantees the edge mode, while the vanishing effective stiffness drives its single-particle confinement, dynamically decoupling the boundary mass from the bulk as the local resonators counterbalance its inertia. This ideal IPR = 1 is a small-amplitude linear limit and thus a concrete design target for extreme localization. In addition to enabling the SPM, we suggest that the identification of such edge modes in locally resonant metamaterials may have advantages when low-frequency operation is required in the face of other requirements, such as quasi-static stiffness. By achieving the SPM below the first Bragg gap—and potentially even in the sub-Bragg regime—we demonstrate an edge mode that inherits two advantages of LRGs: low frequency and unbounded attenuation.

Finally, we addressed practical realizability through boundary tuning. By matching the boundary resonance to the bulk singularity, the SPM can be "pinned" to the zero-effective-stiffness condition over a continuous parameter range rather than at a single fine-tuned point. These tuned states exhibit remarkable resilience against random disorder, provided they remain spectrally separated from the bulk bands.

Beyond the theoretical framework presented here, the proposed system can be realized experimentally by combining two experimentally demonstrated components: four-bar-linkage cells and out-of-plane local resonators. For example, four-bar-linkage cells were fabricated and dynamically tested for longitudinal stress-wave propagation[35,36], and double-lever resonators have been experimentally verified to produce out-of-plane local resonance in locally resonant metamaterials[37]. The main practical challenges are the integration of these components and the control of experimental imperfections, mainly damping and assembly errors[35–37].

More broadly, the underlying physics—a frequency-dependent effective parameter shaped by local resonance—is not specific to the truss-based unit cell and has been experimentally realized in acoustic Helmholtz-resonator metamaterials[3], single-phase elastic chiral metamaterials[38], and electromagnetic split-ring (LC-)resonator metamaterials[39]. The discrete lumped-mass realization is what makes the single-particle (IPR = 1) limit well-defined, but the more general singularity-migration phenomenon can be sought across these platforms. Looking ahead, extending this single-particle localization to prescribed locations within the bulk, and to two-dimensional lattices for reconfigurable waveguiding, may be promising directions for future work.

Methods

Unit-cell dynamics and effective model

We derive here the equations of motion, the dynamical matrix, and the effective-medium description of the system introduced at the beginning of the Results section [Fig. 1d]. The linearized equations of motion governing the jth unit cell are given by:

$$M\ddot{U}_{1,j} + K_1(U_{1,j} - U_{2,j}) + K_2(U_{1,j} - U_{2,j-1}) - k_3\lambda\left[v_{3,j} + \frac{\lambda}{2}(U_{2,j} - U_{1,j})\right] = 0, \tag{13}$$

$$M\ddot{U}_{2,j} + K_1(U_{2,j} - U_{1,j}) + K_2(U_{2,j} - U_{1,j+1}) + k_3\lambda\left[v_{3,j} + \frac{\lambda}{2}(U_{2,j} - U_{1,j})\right] = 0, \tag{14}$$

$$m_3\ddot{v}_{3,j} + k_3\left[v_{3,j} + \frac{\lambda}{2}(U_{2,j} - U_{1,j})\right] = 0, \tag{15}$$

where $\lambda = L/D$ characterizes the geometry of the truss mechanism, relating the horizontal displacement of the primary masses to the vertical displacement of the resonator (see the Supplementary Information section 'Equations of motion and dynamical matrices' for geometric details). The terms involving $k_3\lambda$ represent the coupling forces transmitted through the truss mechanism.

Applying Bloch's theorem with the ansatz $[U_{1,j}, U_{2,j}, v_{3,j}]^T = [U_1, U_2, v_3]^T e^{i(qj-\omega t)}$ transforms these equations into a 3×3 eigenvalue problem, $\mathbf{D}(q)\mathbf{U} = \omega^2\mathbf{U}$, where $\mathbf{U} = [U_1, U_2, \sqrt{2m_3/M}v_3]^T$ is the eigenvector of modal amplitudes. Here, U_1, U_2, and v_3 denote the Bloch amplitudes corresponding to $U_{1,j}$, $U_{2,j}$, and $v_{3,j}$, respectively; the factor $\sqrt{2m_3/M}$ is included to make $\mathbf{D}(q)$ Hermitian. The full dynamical matrix $\mathbf{D}(q)$ is:

$$\mathbf{D}(q) = \begin{pmatrix} \frac{K_1+K_2}{M} + \frac{k_3\lambda^2}{2M} & -\left(\frac{K_1}{M} + \frac{K_2}{M}e^{-iq} + \frac{k_3\lambda^2}{2M}\right) & -\frac{k_3\lambda}{\sqrt{2Mm_3}} \\ -\left(\frac{K_1}{M} + \frac{K_2}{M}e^{iq} + \frac{k_3\lambda^2}{2M}\right) & \frac{K_1+K_2}{M} + \frac{k_3\lambda^2}{2M} & \frac{k_3\lambda}{\sqrt{2Mm_3}} \\ -\frac{k_3\lambda}{\sqrt{2Mm_3}} & \frac{k_3\lambda}{\sqrt{2Mm_3}} & \frac{k_3}{m_3} \end{pmatrix}, \tag{16}$$

where $q = \tilde{\nu}d$ is the normalized wavenumber, d is the lattice constant, and $\tilde{\nu}$ is the physical wavenumber. The diagonal elements represent on-site stiffness contributions, while the off-diagonal elements encode coupling between degrees of freedom (DoF).

To facilitate comparison with a standard stiffness dimer and gain deeper physical insight, we employ an effective medium framework. The local resonator dynamics [Eq. (15)] can be solved algebraically for harmonic motion at frequency ω:

$$v_3 = -\frac{\lambda}{2}\frac{\omega_r^2}{\omega_r^2 - \omega^2}(U_2 - U_1), \tag{17}$$

where $\omega_r = \sqrt{k_3/m_3}$ is the natural frequency of the local resonators. Substituting this back into Eqs. (13) and (14), the entire intracell mechanical structure can be described by a single, frequency-dependent effective stiffness $K_{1,\text{eff}}(\omega)$. Following ref. 25:

$$K_{1,\text{eff}}(\omega) = K_1 + \frac{\lambda^2 k_3}{2}\frac{\omega^2}{\omega^2 - \omega_r^2}. \tag{18}$$

Equation (18) captures the essential physics: below resonance ($\omega < \omega_r$), the second term is negative and reduces the effective stiffness; above resonance ($\omega > \omega_r$), it is positive and increases the stiffness. At $\omega = \omega_r$, the effective stiffness diverges ($K_{1,\text{eff}} \to \pm\infty$); it vanishes ($K_{1,\text{eff}} = 0$) at a distinct frequency $\omega_s < \omega_r$, derived in the Results subsection 'Band gap characterization and switching'.

By substituting Eq. (18), the 3-DoF system reduces to an effective 2-DoF model:

$$M\ddot{U}_{1,j} + K_{1,\text{eff}}(\omega)(U_{1,j} - U_{2,j}) + K_2(U_{1,j} - U_{2,j-1}) = 0, \tag{19}$$

$$M\ddot{U}_{2,j} + K_{1,\text{eff}}(\omega)(U_{2,j} - U_{1,j}) + K_2(U_{2,j} - U_{1,j+1}) = 0. \tag{20}$$

Applying Bloch's theorem yields a 2×2 eigenvalue problem, $\mathbf{D}_{\text{eff}}(q, \omega)\mathbf{U}_{\text{eff}} = \omega^2\mathbf{U}_{\text{eff}}$, where $\mathbf{U}_{\text{eff}} = [U_1, U_2]^T$ and:

$$\mathbf{D}_{\text{eff}}(q, \omega) = \frac{1}{M}\begin{pmatrix} K_{1,\text{eff}} + K_2 & -(K_{1,\text{eff}} + K_2 e^{-iq}) \\ -(K_{1,\text{eff}} + K_2 e^{iq}) & K_{1,\text{eff}} + K_2 \end{pmatrix}. \tag{21}$$

This 2×2 formulation is structurally identical to the standard SSH model, with the crucial difference that $K_{1,\text{eff}}$ is frequency dependent. The band structure nonetheless remains well defined at fixed structural parameters; the full 3×3 Bloch dynamical matrix [Eq. (16)] contains no frequency-dependent parameters and yields these bands directly as a standard linear eigenvalue problem. The frequency dependence of $K_{1,\text{eff}}$ arises only from eliminating the resonator coordinate; the resulting 2×2 form [Eq. (21)] is implicit in ω but, solved self-consistently, reproduces the same bands.

Finite-chain eigenvalue problem

The equation of motion for the finite system of N unit cells with fixed boundaries is:

$$(\mathbf{D}_{3N\times 3N} - \omega^2 \mathbf{I}_{3N\times 3N})\mathbf{u}_{3N\times 1} = \mathbf{0}_{3N\times 1}, \tag{22}$$

where the state vector is $\mathbf{u}_{3N\times 1} = [U_{1,1}, \ldots, U_{1,N}, U_{2,1}, \ldots, U_{2,N}, v_{3,1}, \ldots, v_{3,N}]^T$. The finite dynamical matrix is constructed as $\mathbf{D}_{3N\times 3N} = \mathbf{M}^{-1}_{3N\times 3N}\mathbf{K}_{3N\times 3N}$. The stiffness and mass matrices are given by:

$$\mathbf{K}_{3N\times 3N} = \begin{pmatrix} \mathbf{K}_{11} & \mathbf{K}_{12} & \mathbf{K}_{13} \\ \mathbf{K}_{12}^T & \mathbf{K}_{22} & \mathbf{K}_{23} \\ \mathbf{K}_{13}^T & \mathbf{K}_{23}^T & \mathbf{K}_{33} \end{pmatrix}, \quad \mathbf{M}_{3N\times 3N} = \begin{pmatrix} \mathbf{M}_{11} & \mathbf{0} & \mathbf{0} \\ \mathbf{0} & \mathbf{M}_{22} & \mathbf{0} \\ \mathbf{0} & \mathbf{0} & \mathbf{M}_{33} \end{pmatrix}, \tag{23}$$

where the sub-matrices are defined as:

$$\begin{aligned} &\mathbf{K}_{11} = \mathbf{K}_{22} = \left(K_1 + K_2 + \tfrac{k_3\lambda^2}{2}\right)\mathbf{I}_{N\times N}, \\ &\mathbf{K}_{12} = \begin{pmatrix} \mathbf{0}_{1\times(N-1)} & 0 \\ -K_2\mathbf{I}_{(N-1)\times(N-1)} & \mathbf{0}_{(N-1)\times 1} \end{pmatrix} - \left(K_1 + \tfrac{k_3\lambda^2}{2}\right)\mathbf{I}_{N\times N}, \\ &\mathbf{K}_{13} = -\mathbf{K}_{23} = -k_3\lambda\mathbf{I}_{N\times N}, \quad \mathbf{K}_{33} = 2k_3\mathbf{I}_{N\times N}, \\ &\mathbf{M}_{11} = \mathbf{M}_{22} = M\mathbf{I}_{N\times N}, \quad \mathbf{M}_{33} = 2m_3\mathbf{I}_{N\times N}. \end{aligned} \tag{24}$$

Here, $\mathbf{I}_{N\times N}$ is the identity matrix and $\mathbf{0}$ represents zero matrices of appropriate dimensions.

The spatial localization of an eigenmode is quantified by the inverse participation ratio (IPR), computed over the primary masses:

$$\mathrm{IPR} = \frac{\sum_{j=1}^{N}(U_{1,j}^4 + U_{2,j}^4)}{\left(\sum_{j=1}^{N}(U_{1,j}^2 + U_{2,j}^2)\right)^2}. \tag{25}$$

Disorder modeling

Random disorder is introduced by assigning independent random variations to every stiffness element in the finite chain (K_1, K_2, and k_3) according to the following scheme:

$$K_{1,j} = K(1-\delta) + \Delta \cdot K_r^{(1,j)}, \tag{26}$$

$$K_{2,j} = K(1+\delta) + \Delta \cdot K_r^{(2,j)}, \tag{27}$$

$$k_{3,j} = k_3\left(1 + \frac{\Delta \cdot K_r^{(3,j)}}{K}\right), \tag{28}$$

where $K_r^{(\cdot,j)}$ are random numbers drawn from a uniform distribution over the interval $(-K, K)$, and $\Delta \in [0, 1)$ represents the disorder strength (e.g., $\Delta = 0.1$ corresponds to 10% disorder).

Data availability

The datasets generated and analyzed during the current study are not publicly available due to their being numerical simulation outputs that can be readily reproduced from the model equations and parameter values specified in the Methods and figure captions, but are available from the corresponding author on reasonable request.

Code availability

The custom MATLAB (R2022a) scripts used to compute the band structures, Zak phases, finite-chain eigenspectra, and disorder analyses are not publicly available as they are part of an ongoing study, but are available from the corresponding author on reasonable request. All model parameters required to reproduce the results are specified in the Methods and figure captions.

Received: 17 January 2026; Accepted: 9 June 2026;
Published online: 05 November 2026

References

1. Lu, M.-H., Feng, L. & Chen, Y.-F. Phononic crystals and acoustic metamaterials. *Mater. Today* **12**, 34–42 (2009).
2. Li, J. & Chan, C. T. Double-negative acoustic metamaterial. *Phys. Rev. E* **70**, 055602 (2004).
3. Fang, N. et al. Ultrasonic metamaterials with negative modulus. *Nat. Mater.* **5**, 452–456 (2006).
4. Chan, C. T., Li, J. & Fung, K. H. On extending the concept of double negativity to acoustic waves. *J. Zhejiang Univ. Sci. A* **7**, 24–28 (2006).
5. Ding, Y., Liu, Z., Qiu, C. & Shi, J. Metamaterial with simultaneously negative bulk modulus and mass density. *Phys. Rev. Lett.* **99**, 093904 (2007).
6. Lee, S. H. & Wright, O. B. Origin of negative density and modulus in acoustic metamaterials. *Phys. Rev. B* **93**, 024302 (2016).
7. Wang, X. Dynamic behaviour of a metamaterial system with negative mass and modulus. *Int. J. Solids Struct.* **51**, 1534–1541 (2014).
8. Liu, L. & Hussein, M. I. Wave motion in periodic flexural beams and characterization of the transition between bragg scattering and local resonance. *J. Appl. Mech.* **79**, 011003 https://doi.org/10.1115/1.4004592 (2011).
9. Theocharis, G., Richoux, O., García, V. R., Merkel, A. & Tournat, V. Limits of slow sound propagation and transparency in lossy, locally resonant periodic structures. *New J. Phys.* **16**, 093017 (2014).
10. Lin, Q., Zhou, J., Pan, H., Xu, D. & Wen, G. Numerical and experimental investigations on tunable low-frequency locally resonant metamaterials. *Acta Mech. Solid. Sin.* **34**, 612–623 (2021).
11. Achaoui, Y., Khelif, A., Benchabane, S., Robert, L. & Laude, V. Experimental observation of locally-resonant and bragg band gaps for surface guided waves in a phononic crystal of pillars. *Phys. Rev. B Condens. Matter. Mater. Phys.* **83**, 104201 (2011).
12. Jamil, F., Chen, F., Deng, B., Parker, R. G. & Wang, P. Inerter-based elastic metamaterials for band gap at extremely low frequency. *Extrem. Mech. Lett.* **56**, 101847 (2022).
13. Raghavan, L. & Phani, A. S. Local resonance bandgaps in periodic media: Theory and experiment. *J. Acoust. Soc. Am.* **134**, 1950–1959 (2013).
14. Liu, Y., Chen, X. & Xu, Y. Topological phononics: from fundamental models to real materials. *Adv. Funct. Mater.* **30**, 1904784 (2020).
15. Shah, T., Brendel, C., Peano, V. & Marquardt, F. Colloquium: topologically protected transport in engineered mechanical systems. *Rev. Mod. Phys.* **96**, 021002 https://doi.org/10.1103/RevModPhys.96.021002 (2024).
16. Wang, P., Lu, L. & Bertoldi, K. Topological phononic crystals with one-way elastic edge waves. *Phys. Rev. Lett.* **115**, 104302 https://doi.org/10.1103/PhysRevLett.115.104302 (2015).
17. Mousavi, S. H., Khanikaev, A. B. & Wang, Z. Topologically protected elastic waves in phononic metamaterials. *Nat. Commun.* **6**, 8682 (2015).
18. Serra-Garcia, M. et al. Observation of a phononic quadrupole topological insulator. *Nature* **555**, 342–345 https://doi.org/10.1038/nature25156 (2018).
19. Zhang, Q., Chen, Y., Zhang, K. & Hu, G. Dirac degeneracy and elastic topological valley modes induced by local resonant states. *Phys. Rev. B* **101**, 014101 (2020).
20. Xia, Y., Erturk, A. & Ruzzene, M. Topological edge states in quasiperiodic locally resonant metastructures. *Phys. Rev. Appl.* **13**, 014023 (2020).
21. Sugino, C., Leadenham, S., Ruzzene, M. & Erturk, A. On the mechanism of bandgap formation in locally resonant finite elastic metamaterials. *J. Appl. Phys.* **120**, 134501 (2016).

22. Zhao, D., Xiao, M., Ling, C. W., Chan, C. T. & Fung, K. H. Topological interface modes in local resonant acoustic systems. *Phys. Rev. B* **98**, 014110 (2018).
23. Jang, Y., Kim, S., Kim, E. & Rho, J. Singular topological edge states in locally resonant metamaterials. *Sci. Bull*. **70**, 1080–1086, https://doi.org/10.1016/j.scib.2025.01.010 (2025).
24. Zhang, H., Tang, L., Hu, G., Li, Y. & Aw, K. Realization of topological Bragg and locally resonant interface states in one-dimensional metamaterial beam-resonator-foundation system. *J. Phys. D Appl. Phys.* **57**, 505304 (2024).
25. Huang, H. & Sun, C. Theoretical investigation of the behavior of an acoustic metamaterial with extreme Young's modulus. *J. Mech. Phys. Solids* **59**, 2070–2081 (2011).
26. Kaina, N., Fink, M. & Lerosey, G. Composite media mixing Bragg and local resonances for highly attenuating and broad bandgaps. *Sci. Rep.* **3**, 3240 (2013).
27. Leykam, D., Andreanov, A. & Flach, S. Artificial flat band systems: from lattice models to experiments. *Adv. Phys. X* **3**, 1473052 https://doi.org/10.1080/23746149.2018.1473052 (2018).
28. Banerjee, A., Adhikari, S. & Hussein, M. I. Inertial amplification band-gap generation by coupling a levered mass with a locally resonant mass. *Int. J. Mech. Sci.* **207**, 106630 (2021).
29. Frandsen, N. M., Bilal, O. R., Jensen, J. S. & Hussein, M. I. Inertial amplification of continuous structures: large band gaps from small masses. *J. Appl. Phys.* **119**, 124902 (2016).
30. Vanderbilt, D. *Berry Phases in Electronic Structure Theory: Electric Polarization, Orbital Magnetization and Topological Insulators* (Cambridge University Press, 2018).
31. Xiao, M., Zhang, Z. & Chan, C. T. Surface impedance and bulk band geometric phases in one-dimensional systems. *Phys. Rev. X* **4**, 021017 (2014).
32. Asbóth, J. K., Oroszlány, L. & Pályi, A. A short course on topological insulators. *Lecture Notes in Physics*, Vol. 919, https://doi.org/10.1007/978-3-319-25607-8 (Springer, 2016).
33. Huang, H.-H., Sun, C.-T. & Huang, G. On the negative effective mass density in acoustic metamaterials. *Int. J. Eng. Sci.* **47**, 610–617 (2009).
34. Al Ba'ba'a, H. B., Yousef, H. & Nouh, M. A blueprint for truncation resonance placement in elastic diatomic lattices with unit cell asymmetry. *JASA Express Lett.* **4**, 077501, https://doi.org/10.1121/10.0027939 (2024)
35. Zhou, W., Li, Y., Yan, G. & Zhou, J. Quasi-full bandgap generating mechanism by coupling negative stiffness and inertial amplification. *Eur. J. Mech. A Solids* **103**, 105143 (2024).
36. Taniker, S. & Yilmaz, C. Generating ultra wide vibration stop bands by a novel inertial amplification mechanism topology with flexure hinges. *Int. J. Solids Struct.* **106**, 129–138 (2017).
37. Pires, F. A. et al. Novel resonator concept for improved performance of locally resonant based metamaterials. *Thin Walled Struct.* **209**, 112866 (2025).
38. Zhu, R., Liu, X., Hu, G., Sun, C.-T. & Huang, G. Negative refraction of elastic waves at the deep-subwavelength scale in a single-phase metamaterial. *Nat. Commun.* **5**, 5510 (2014).
39. Smith, D. R., Padilla, W. J., Vier, D. C., Nemat-Nasser, S. C. & Schultz, S. Composite medium with simultaneously negative permeability and permittivity. *Phys. Rev. Lett.* **84**, 4184 (2000).

Acknowledgements

G.S.S. acknowledges financial support through the Prime Minister's Research Fellowship (PMRF ID: 0202572). R.C. gratefully acknowledges support from the Indian Institute of Science Startup Grant. K.Q. and N.B. acknowledge support from the U.S. Army Research Office (Grant No. W911NF-20-2-0182). I.F. acknowledges support from the Department of Defense (DoD) through the National Defense Science & Engineering Graduate (NDSEG) Fellowship Program. Finally, G.S.S. thanks his late mother, Mrs. Lakshmi, for her support and encouragement during the early stages of this work.

Author contributions

G.S.S., K.Q. and I.F. performed theoretical and numerical analyses. G.T., N.B. and R.C. supervised the work. All authors discussed the results and contributed to the manuscript. G.S.S., K.Q. and I.F. contributed equally to this work.

Competing interests

N.B. is a founder and holds equity positions in Euler Materials. G.T. is a Guest Editor of the npj Acoustics Collection "Harnessing Topology in Acoustics: Advances in Sound Control and Manipulation''. G.T. was not involved in the journal's review of, or decisions related to, this manuscript. The other authors do not have a competing interest.

Additional information

Supplementary information The online version contains supplementary material available at https://doi.org/10.1038/s44384-026-00078-1.

Correspondence and requests for materials should be addressed to Rajesh Chaunsali.

Reprints and permissions information is available at http://www.nature.com/reprints

Publisher's note Springer Nature remains neutral with regard to jurisdictional claims in published maps and institutional affiliations.

Open Access This article is licensed under a Creative Commons Attribution-NonCommercial-NoDerivatives 4.0 International License, which permits any non-commercial use, sharing, distribution and reproduction in any medium or format, as long as you give appropriate credit to the original author(s) and the source, provide a link to the Creative Commons licence, and indicate if you modified the licensed material. You do not have permission under this licence to share adapted material derived from this article or parts of it. The images or other third party material in this article are included in the article's Creative Commons licence, unless indicated otherwise in a credit line to the material. If material is not included in the article's Creative Commons licence and your intended use is not permitted by statutory regulation or exceeds the permitted use, you will need to obtain permission directly from the copyright holder. To view a copy of this licence, visit http://creativecommons.org/licenses/by-nc-nd/4.0/.

© The Author(s) 2026